Earth and Planetary Science Letters 592 (2022) 117618

Contents lists available at ScienceDirect

Earth and Planetary Science Letters

www.elsevier.com/locate/epsl

What causes the spatiotemporal patterns of seismicity in the Three Gorges Reservoir area, central China?

Linxuan Li [a], Gang Luo [a,b,c,*]

[a] School of Geodesy and Geomatics, Wuhan University, 129 Luoyu Road, Wuhan 430079, China
[b] Key Laboratory of Geospace Environment and Geodesy, Ministry of Education, Wuhan University, 129 Luoyu Road, Wuhan 430079, China
[c] Hubei Luojia Laboratory, 129 Luoyu Road, Wuhan 430079, China

ARTICLE INFO

Article history:
Received 27 December 2021
Received in revised form 25 April 2022
Accepted 13 May 2022
Available online 25 May 2022
Editor: J.P. Avouac

Keywords:
Three Gorges Reservoir
water-level fluctuation
seasonal precipitation
spatiotemporal seismicity patterns
seasonal seismicity

ABSTRACT

Both artificial and natural hydrosphere changes can impact regional seismicity. In the Three Gorges Reservoir (TGR) area, because of human regulation, the reservoir water level and natural rainfall show opposite seasonal patterns: when the reservoir water level is high, the precipitation amount is low, and vice versa. To investigate whether these artificial and natural factors are related to regional spatiotemporal seismicity and, if they are, to reveal the possible mechanisms, we used statistical analysis and calculated changes in stresses and pore fluid pressures due to these factors. We found that, based on the distances of the epicenters to the TGR, earthquakes can be divided into two groups: those occurring within 0–12 km and those occurring within 32–70 km. Our results show that the reservoir water-level fluctuation influences the seismicity near the TGR (0–12 km), resulting in fewer earthquakes in summer and more in winter. Stress changes caused by the elastic response to water loading play an important role in this trend. In contrast to the seasonal pattern of near-TGR seismicity, earthquakes far from the TGR (32–70 km), to some extent, show opposite pattern: more in summer and less in winter. Furthermore, we found that seismic productivity far from the TGR (32–70 km) is moderately correlated with seasonal precipitation. But it cannot be explained by the precipitation-induced pore pressure variations.

1. Introduction

Hydrosphere changes can either promote or inhibit regional seismicity. These changes can be attributed to human and natural factors, such as reservoir impoundment, oil and gas production, wastewater injection, river-level fluctuation, rainfall, and snow (Ader and Avouac, 2013; Bettinelli et al., 2008; Craig et al., 2017; Dutilleul et al., 2021; Ge et al., 2009; Gonzalez et al., 2012; Johnson et al., 2017a; Keranen et al., 2014; Perry and Bendick, 2021; Talwani et al., 2007; Xue et al., 2020). Generally, hydrosphere changes can be associated with seismicity as they may cause changes in regional stress field and pore fluid pressure. To be more specific, first, the mass redistribution will change the regional stress field. If this change overcomes the frictional strength of a pre-existing fault, an earthquake can be triggered (e.g., Foulger et al., 2018; Xue et al., 2020). Second, the instantaneous response (undrained effect) and the diffusion of water may increase the pore fluid pressure on some pre-existing faults, reduce the effective normal stress, and cause sudden fault sliding (e.g., Ge et al., 2009; Talwani et al., 2007).

Around the Three Gorges Reservoir (TGR) in central China, hydrosphere changes are influenced by both artificial and natural factors, making it ideal for investigating the relationship between regional seismicity and hydrosphere changes. The TGR was created in 2003 due to the construction of the Three Gorges Dam (TGD) on the Yangtze River, the largest hydropower dam in the world (Fig. 1). The TGR extends westward from the TGD, with a length of approximately 660 km and a water area of approximately 1,040 km^2 (Wang et al., 2013). In contrast to natural conditions, the rainy season corresponds to the low-water-level period of the reservoir (Tang et al., 2019; Xue et al., 2020; Fig. 2a and 2b). The TGR area is situated in the transition zone from the Tibetan Plateau to the hills and plains of eastern China. It has a complex geological and tectonic background with multiple active faults, such as Xiannvshan Fault (XNF) and Huayingshan Fault (HYF) (Fig. 1), and can host moderate-sized earthquakes (Huang et al., 2018; Tang et al., 2019; Zhang and Lou, 2011).

Abbreviations: 1D, one-dimensional; AF, Allan factor; ECA, earthquake concentration area; EQ, earthquakes; GNSS, Global Navigation Satellite System; HYF, Huayingshan Fault; ITS, injection-triggered seismicity; MCSD, maximum compressive stress direction; TGD, Three Gorges Dam; TGR, Three Gorges Reservoir; XNF, Xiannvshan Fault.

* Corresponding author at: School of Geodesy and Geomatics, Wuhan University, 129 Luoyu Road, Wuhan 430079, China.
E-mail addresses: gluo@sgg.whu.edu.cn, gangluo66@gmail.com (G. Luo).

https://doi.org/10.1016/j.epsl.2022.117618
0012-821X/

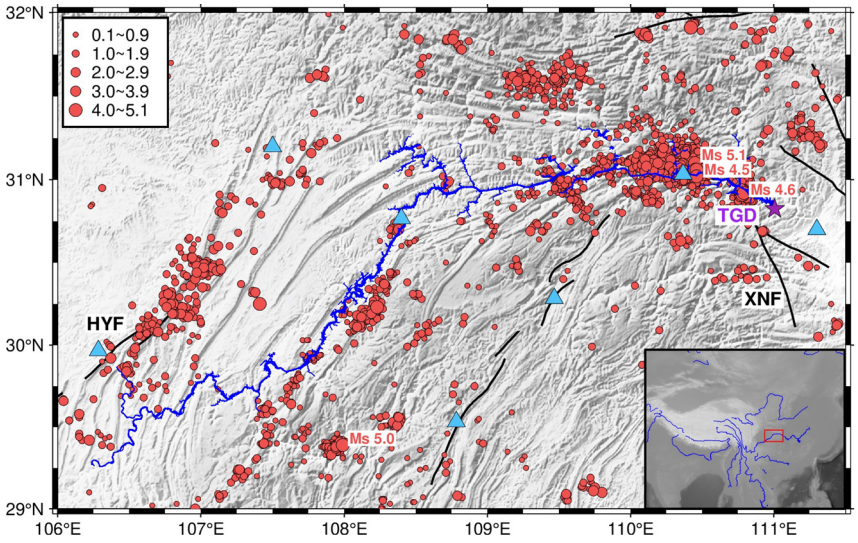

Fig. 1. Map of the Three Gorges Reservoir area. Regional earthquakes (2009–2020) are marked as red circles sized by magnitude. The largest four earthquakes are 2013 Ms 5.1, 2017 Ms 5.0, 2014 Ms 4.6, and 2014 Ms 4.5. Black lines represent the faults, and the two main active faults, Xiannvshan Fault (XNF) and Huayingshan Fault (HYF), are marked. Light blue triangles show the locations of the seven selected meteorological stations. The Three Gorges Dam (TGD) is marked by purple stars. (For interpretation of the colors in the figures, the reader is referred to the web version of this article.)

Since its first impoundment, many surveys on seismicity have been conducted in the head area of the reservoir (within several tens of kilometers near the TGD). Many researchers have claimed that impoundment has a significant impact on regional seismicity (e.g., Huang et al., 2018; Wu et al., 2012; Yi et al., 2012; Zhang et al., 2018). However, there is currently little research on the spatiotemporal patterns and mechanisms of seismicity over the entire TGR area. In addition, the TGR area is located in the Yangtze paraplatform; hence, more studies on its seismicity can help elucidate the seismic response to surface processes, the mechanisms of intraplate seismicity, and the physical processes of induced earthquakes.

In this study, we first collected data on seismicity, reservoir water level, and regional precipitation in the TGR area since the third stage of impoundment (2009–2020). We then investigated the temporal patterns of regional seismicity and their relationship with hydrosphere changes using statistical analysis. To elucidate the underlying mechanisms, we calculated stress changes and pore pressure variations due to water-level changes and seasonal precipitation, respectively.

2. Data

2.1. Water-level data and precipitation data

The daily water-level data measured in front of the TGD since 2003 was downloaded from the Yangtze River Hydrological Network. Considering the large fluctuation in the autumn of 2020, we focused on the 11 storage cycles between July 2009 and June 2020 in the following analysis (Figs. S1 and 2a-1). To show the seasonal pattern of the water level, we calculated the average water level in the 11 storage cycles with a step width of one day (Fig. 2a-2). The data of seasonal water volume changes in the TGR water area were from Lai et al. (2022). They were obtained from the Shuttle Radar Topography Mission digital elevation model v4.1 with a spatial resolution of 90 m (Lai et al., 2022).

Daily precipitation data from seven stations in the TGR area from 2009 to 2020 were collected from the China Meteorological Data Service Center (Figs. 1 and S2a). We calculated the monthly precipitation at each station based on the unevenness of the month length (adjusting the precipitation assuming that there were 31 days in each month) and found a consistent annual signal (Fig. S2b). Therefore, we assumed that the spatial variability of precipitation is negligible compared to the uncertainty of the regional geological structure. We then calculated the precipitation time series of the area using the average of the data from the seven stations (Fig. 2b-1). The precipitation time series obtained between 11 water storage cycles was averaged to generate the average monthly precipitation in the TGR area (Fig. 2b-2).

2.2. Earthquake catalog and declustering

We collected seismic catalog data for the region (106°E–111.5°E, 29°N–32°N) from the China Earthquake Network (China Unified Earthquake Catalog). The data were compiled by the China Earthquake Administration using the results produced by local networks (below M 4) and the national network (above M 4). They include 3,224 events with $M > 0$ from January 1, 2009, to December 31, 2020 (Fig. 1). The magnitude of completeness (Mc) was estimated to be 1.2 (Fig. S3a). We used the nearest-neighbor distance approach (Zaliapin and Ben-Zion, 2013) to identify and remove clusters of aftershocks from the catalog (Figs. S3 and 2c-1). In the following analysis, we used the declustered catalog directly without considering the minimum complete magnitude. This is because the declustered catalog includes 2,388 events during the 11 water storage cycles. However, under the constraint of the minimum complete magnitude, the number of earthquakes is reduced to 809, which is not conducive to statistical analysis (Fig. S5; Craig et al., 2017; Xue et al., 2020). We then adjusted the number of earthquakes in each month according to the unevenness of the month length and stacked them annually (Fig. 2c-2).

3. Methods

3.1. Statistical analysis

We first analyzed the spatial distribution of declustered earthquakes and divided them into two groups according to the distances of the epicenters to the TGR. Based on the statistical approaches described below, we then investigated their temporal patterns, differences, and relationships with hydrosphere changes.

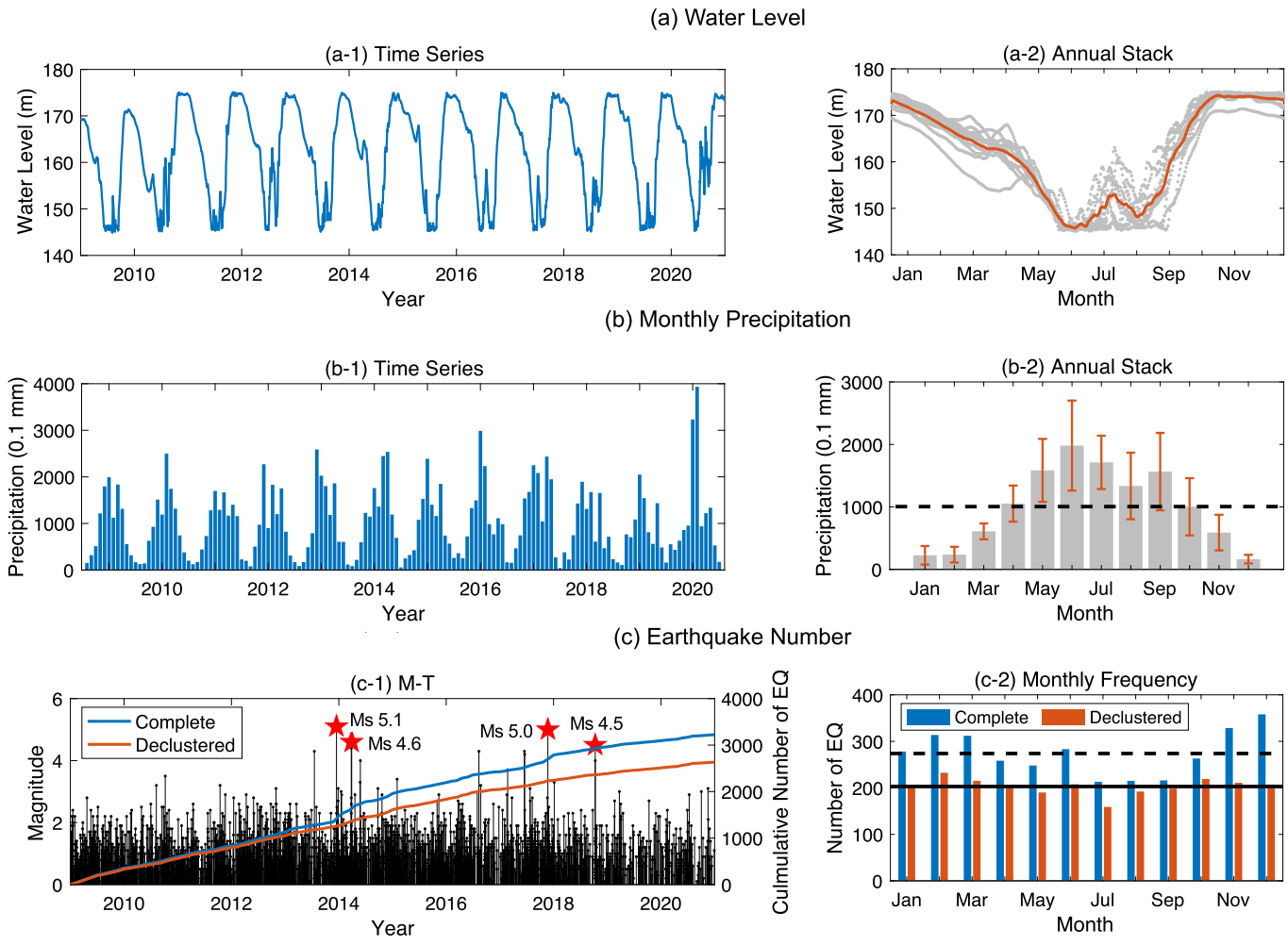

Fig. 2. Comparison among water level, precipitation, and seismicity. (a-1) Time series of TGR water level at the TGD from January 1, 2009, to December 31, 2020. (a-2) Water level from July 1, 2009, to June 30, 2020, stacked on an annual timescale with 1 day running average (orange). (b-1) Monthly precipitation in the TGR area from January 2009 to December 2020. (b-2) Monthly precipitation histogram from July 2009 to June 2020, stacked on an annual timescale with 1-standard deviation (orange bars). Dotted horizontal line shows average monthly precipitation. (c-1) The cumulative number of earthquakes (EQ) for the complete (blue curve) and declustered (orange curve) catalogs from January 1, 2009, to December 31, 2020. The event magnitudes of the complete catalog are indicated by black bars. (c-2) Earthquake frequency histogram of complete (blue bars) and declustered (orange bars) catalogs from July 2009 to June 2020, stacked on an annual timescale. Dotted and solid horizontal lines show the average values for the complete and declustered catalogs, respectively.

The clustering of earthquakes over time is shown by the coefficient of variation C_v. It is defined as:

$$C_v = \frac{\sigma}{\mu}, \tag{1}$$

where σ and μ are the standard deviation and the mean value of the event interval time, respectively. The earthquake sequence is regular if C_v is lower than 1, Poissonian if C_v is 1, or clustered if C_v is greater than 1 (Kagan and Jackson, 1991).

C_v provides the time-cluster information of the point process but does not reveal its timescale. Therefore, we used the Allan factor (*AF*) and Schuster spectra, which have different resolutions and sensitivities, to determine seismic periodicity.

AF is related to the variability in successive counts (Thurner et al., 1997). The catalog is divided by duration τ, and a counting sequence of earthquakes is obtained. The number of earthquakes falling in the k^{th} window is shown by $N_k(\tau)$. Then, *AF* is defined as

$$AF(\tau) = \frac{\left\langle \left(N_{k+1}(\tau) - N_k(\tau)\right)^2 \right\rangle}{2\left\langle N_k(\tau)\right\rangle}, \tag{2}$$

where $\langle x \rangle$ denotes the mean value of x. If the process is clustering, the *AF* will change with duration τ. The decline of the logarithmic curve of *AF*-τ on a particular timescale indicates that the earthquake sequence has periodicity on this timescale (Telesca et al., 2017).

The Schuster test regards each earthquake as a unit vector, whose direction is represented by the phase angle (the phase angle of the event that occurs at time t_k is $\theta_k = 2\pi t_k/T$, where T is the periodicity). The vector sum is used to calculate the probability that the concentration of events in the catalog changes according to a sine function (Schuster, 1897). Based on the Schuster test, Schuster spectra is a more reliable periodic detection method, the principle of which is to perform multiple Schuster tests (Ader and Avouac, 2013). Quantitatively, if the p-value is lower than 0.01 T/t (t is the duration of the catalog), we can claim that a periodicity T is detected above the 99% confidence level.

Simultaneously, we employed jackknife analysis on the stacked series. It excludes the data of each storage cycle (July to June of the following year) separately (Craig et al., 2017). By comparing the stacked series after excluding the data for each cycle, we can verify the statistically significant periodicity and assess whether the periodicity is the result of extreme excursions in a single year.

We then aimed to reveal the seasonality and underlying driving mechanisms of these two groups of earthquakes. We used the Pearson and cross-correlation coefficients to test the correlation between earthquake frequency and hydrosphere changes.

3.2. Calculation of elastic stress changes caused by water-level fluctuation

The TGR experiences a rapid 30-m rise in the water level before winter every year from 2009 to 2020 (Fig. 2a). This would lead to an increase of 22.7 km^3 water in the TGR water area (Wang et al., 2013), which can induce changes in the static stress field, and thus, may modulate regional seismicity (e.g., Ge et al., 2009; Xue et al., 2020). Previous studies have usually used the Mohr–Coulomb criterion and calculated changes in the Coulomb failure stress to evaluate the effects of static loading on the stress of a known fault plane and its seismicity (e.g., Ge et al., 2009; Xue et al., 2020). This requires the input of fault parameters, such as strike, dip, and rake. However, in the TGR area, these geometrical parameters of faults, on which seismicity occurred, are not clarified, and some of the earthquakes occurred on unmapped faults. Furthermore, the magnitude of the earthquakes in the TGR area was small, typically M 0–2. Thus, it is impossible to obtain the focal mechanism solution data and derive fault geometry information.

To evaluate the effects of water loading on the regional stress field, we introduced the Drucker–Prager yield criterion (Drucker and Prager, 1952). It includes the effects of the mean stress and shear stress and can be expressed as follows (Drucker and Prager, 1952):

$$F_{DP} = \sqrt{J_2} + \alpha I_1 - \beta, \tag{3}$$

$$\alpha = \frac{2\sin\phi}{\sqrt{3}\,(3+\sin\phi)}, \tag{4}$$

$$\beta = \frac{6C\cos\phi}{\sqrt{3}\,(3+\sin\phi)}, \tag{5}$$

where F_{DP} is the yield stress function under Drucker-Prager criterion, α and β are material constants related to cohesion C and internal friction angle ϕ, I_1 is the first invariant of the stress tensor, and J_2 is the second invariant of the deviatoric stress tensor. In this study, we defined compressional stress as negative. The internal friction angle of dry rock is usually approximately 30°, which decreases if the rock is wetted by water (Byerlee, 1978; Jaeger et al., 2007; Zoback, 2007). Similar to the changes in the Coulomb failure stress, an increase in F_{DP} ($\Delta F_{DP} > 0$) promotes failure, whereas a decline in F_{DP} ($\Delta F_{DP} < 0$) moves the stress state far away from failure and increases the stability of rocks.

A regional initial stress field is required to calculate ΔF_{DP}. However, the TGR area lacks reliable crustal stress observation data, and some inconsistencies exist. For example, a recent tectonic stress map of China shows that the maximum compressive stress direction (MCSD) of the entire TGR area is NW–SE (Hu et al., 2017). In contrast, the MCSD in the head area of the TGR was reported to be NE–SW (Wu et al., 2012). In light of this, we estimated two initial regional stress fields using the method proposed by Zoback (1992) according to these two viewpoints. We then calculated the regional stress field change due to impoundment using Boussinesq's three-dimensional analytical solution (Jaeger et al., 2007). The final regional stress field was calculated by superimposing the stress field change onto the initial regional stress field. Hence, ΔF_{DP} can be calculated by subtracting the initial F_{DP} from the final F_{DP}. More information on the Drucker–Prager yield criterion and calculation is shown in the Supplementary Material (Text S1).

3.3. Calculation of pore pressure changes caused by monthly precipitation

Precipitation can affect regional seismicity by causing changes in pore pressure (Hainzl et al., 2006, 2013). Here, we used a one-dimensional (1D) model (Dutilleul et al., 2021; Hainzl et al., 2013) to assess this effect in the TGR area. The model includes the poroelastic effect (undrained response) and pore pressure diffusion. The change in groundwater level is regarded as the difference between the monthly precipitation and the average value (Dutilleul et al., 2021). More details are provided in the Supplementary Material (Text S2).

4. Results

4.1. Relationship between water level, precipitation, and observed seismicity

From the complete catalog, we observed that seismicity in the TGR area was frequent when the water level reached its highest point and then began to fall (November, December, February, and March; blue bars in Fig. 2c-2). This is consistent with the seismicity observed in the head area of the TGR (Zhang et al., 2018). However, the difference is weakened after declustering (orange bars in Fig. 2c-2). This indicates that earthquakes in winter are more likely to generate aftershocks.

Seismicity in the TGR area exhibited three spatial distribution characteristics (Fig. 3). First, horizontally, the epicenters were mainly distributed within 12 km or between 32 and 70 km from the TGR (Figs. 3a and 3c). We observed this pattern in both the complete catalog and the declustered catalog using Mc = 1.2 as a minimum (Fig. S4). Therefore, this pattern is an inherent feature of regional seismicity rather than a statistical fluke. Second, vertically, the hypocenters of approximately 90% of the events were distributed within 10 km of the surface, and approximately 70% of them occurred 5–7 km below the surface (Figs. 3b and 3c). Finally, earthquakes with deep focal depths typically occurred directly below the TGR or very close to the river bank (within a few kilometers) (Fig. 3c).

We calculated the coefficients of variation for the declustered catalogs of these two groups of earthquakes (located 0–12 km [group-1] and 32–70 km [group-2] away from the TGR, respectively). We obtained $C_v \sim 1.21$ for group-1 and $C_v \sim 1.19$ for group-2. To assess the significance of these results, we randomly generated 10,000 Poisson catalogs of the same size and average seismicity rate for each group. The 95% confidence intervals for Poissonian surrogates are $[0.95, 1.05]$ (group-1) and $[0.92, 1.08]$ (group-2), which suggests that both groups are clustered over the entire time domain at 95% confidence. The irregular clustering indicates potential irregular factors that have an impact on regional seismicity.

The *AF* shows that both groups have periods of slightly more than 1 year and 1.5 years (Fig. 4). The Schuster spectrum shows the annual period for group-1 events, while group-2 events show several periods of less than 1 year, among which the 1-day period may reflect the role of solid tide or the daily changes in detection levels (Fig. 5). Periodicities other than 1 year are interesting. Telesca et al. (2021) and Dutilleul et al. (2021) also reported multiple periodicities in the Song Tranh 2 Reservoir area (Vietnam) and near Parkfield, but failed to determine a mechanism. Therefore, we focused only on the annual cycle, which may be explained by hydrosphere changes. We applied jackknife analysis to two sub-catalogs and verified the annual periodicities (Figs. S5c and S5d). An earthquake swarm was found at 32–70 km in February 2013, which continued to show a clustering characteristic after the nearest-neighbor approach was applied (Fig. S6b). Thus, we

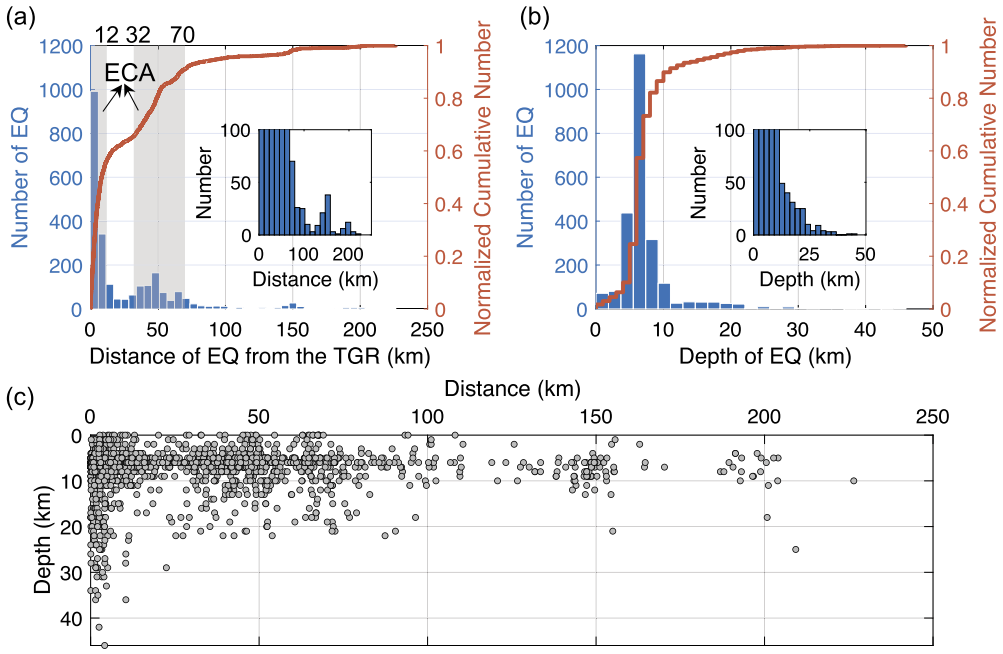

Fig. 3. Distribution characteristics of regional seismicity. (a) Cumulative histogram of earthquakes versus distance from the TGR for the declustered catalog. The gray shading marks two earthquake concentration areas (ECAs), which are respectively bounded by 12 km, 32 km, and 70 km away from the TGR. (b) Cumulative histogram of earthquakes versus depth of the earthquakes for the declustered catalog. (c) The relationship between focal depth and epicenter distance from the TGR (declustered catalog). EQ: earthquakes.

eliminated the swarm-related events that occurred within the region (107.5°E–108.5°E, 29°N–29.5°N) in the following analysis.

The earthquake frequency was stacked for each month, and we found that these two groups of earthquakes do not have the same seasonal characteristics. The productivity of group-1 earthquakes is enhanced in winter and reduced in summer (Fig. 6a). In contrast, the productivity of group-2 earthquakes appears to be enhanced in summer and reduced in winter (Fig. 6b). The correlation coefficient between the monthly number of group-1 earthquakes and the water level was 0.93, indicating a high correlation. Meanwhile, the correlation coefficient between the monthly number of group-2 earthquakes and precipitation was 0.58, showing a moderate correlation. According to the cross-correlation, the frequency of the stacked sequences and changes in the hydrosphere are maintained in synchronization (Fig. S7).

4.2. Water-level fluctuation and monthly rainfall induced stress changes

To help understand the impact of reservoir water-level change on the crust, we first checked the surface deformation using the Global Navigation Satellite System (GNSS) series. We found that the phase of the GNSS series is the same as that of the water level (Figs. S8b–S8d, blue curves). We used Boussinesq's model (Jaeger et al., 2007) to simulate surface deformation and found that the results are consistent with actual observations (Fig. S8). We then calculated the changes in F_{DP} caused by the 30-m rise in water level (Figs. 7a–7d, S9, and S10). When the internal friction angle ϕ is low, the area near or below the reservoir is the concentration area of positive ΔF_{DP}. Generally, the entire area tends to be more stable with a larger internal friction angle ϕ (Figs. S9 and S10). This results from the greater effect of the mean stress on the yield stress. In addition, the absolute value of ΔF_{DP} gradually decreases with depth, but the distribution remains approximately the same (Figs. S9 and S10). We further calculated the ΔF_{DP} at the hypocenters of group-1 earthquakes (Figs. 7e–7i and S11). We found that when $\phi = 0°$, 74% (MCSD: NW–SE) and 66% (MCSD: NE–SW) of the earthquakes occurred in places where ΔF_{DP} was positive. The ratio of earthquakes with positive ΔF_{DP} decreases as ϕ increases (Fig. 7i). This result indicates that the elastic response induced most of the group-1 earthquakes if the internal friction angle is low. We also noticed that deep earthquakes typically had a positive ΔF_{DP} under different ϕ and background stress fields (Figs. 7g, 7h, and S11). This implies that elastic response plays a leading role in the deep part.

To explore the relationship between group-2 events and precipitation, we estimated the seasonal pore pressure changes caused by precipitation. We tested the hydraulic coefficient between 0.1 and 10 m^2/s, which is considered a reasonable range (Talwani et al., 2007). The pore pressure peaked in October, and there is a two- to three-month delay compared with precipitation (Fig. 8). Owing to the coupling of the undrained and diffusion effects, the phase differences at different depths are not obvious (Figs. 8a, 8b, and S12). Overall, the increase in pore pressure has a time lag at all depths (Fig. S12), which cannot match the change in seismic productivity.

5. Discussion

We observed seasonal characteristics of earthquakes closer to the TGR (0–12 km, group-1). The annual stacking form of the sequence shows a high correlation with the reservoir water level. For earthquakes 32–70 km from the TGR (group-2), this annual periodicity and seasonality are weakened and are not evident in the Schuster spectra. The annual stacking form of the sequence shows a moderate correlation with regional precipitation. We are convinced that group-2 events are not synchronized with those in group-1. But we also acknowledge that there is less statistical evidence for seasonal seismicity variations in group-2 events. One possible explanation is that the variations in precipitation are significantly less than that in the reservoir water level, causing the surface mass load to be concentrated in the reservoir rather than in the surrounding area. Thus, seismicity far from the TGR may have a weaker annual periodicity. To demonstrate the robustness of our results, we adjusted the boundaries of these two earthquake groups and observed the same seasonality (Fig. S13). However, we could not observe the seasonality of earthquakes that occurred 32–70 km from the TGR (Fig. S14). Therefore, the TGR area can

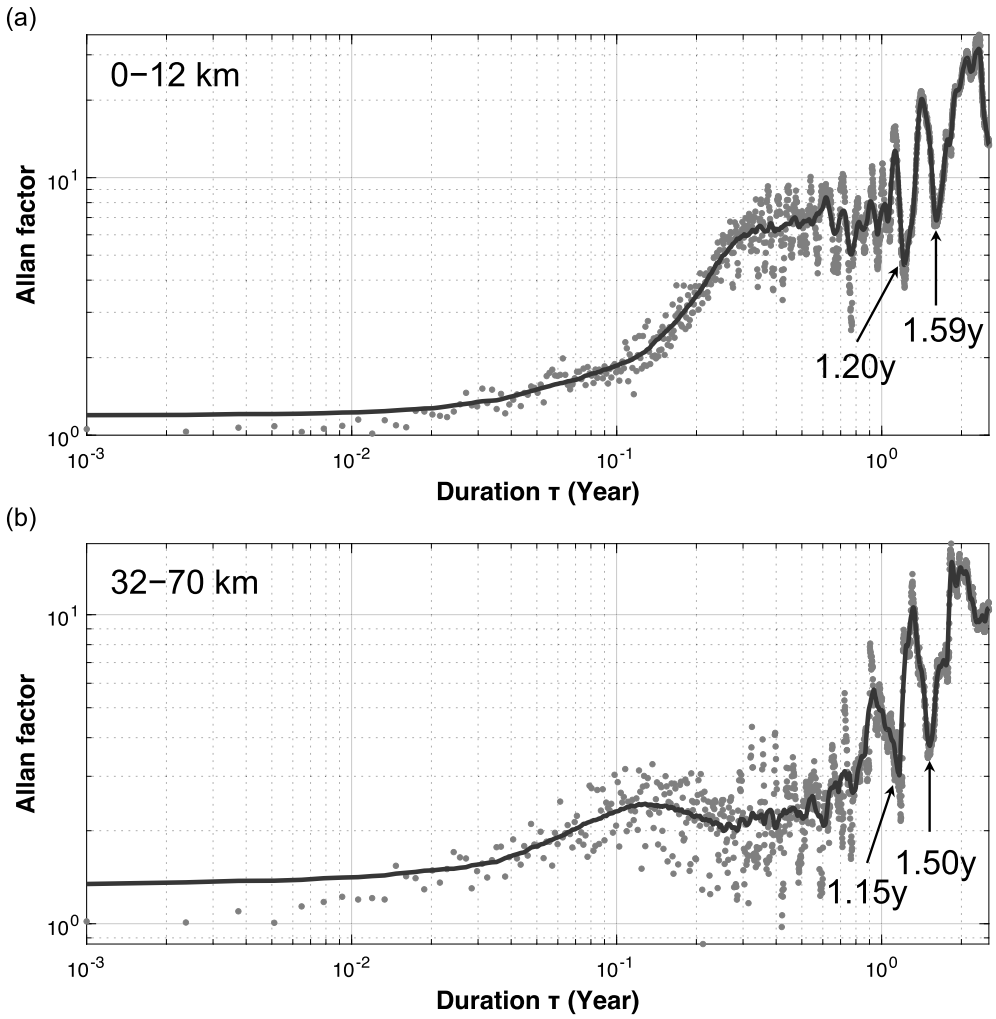

Fig. 4. Allan factor for group-1 (a) and group-2 (b) declustered sub-catalogs. y: year.

indeed be divided into three regions, two of which are earthquake concentration areas (ECAs) with different seismicity patterns.

To evaluate the mechanism of group-1 events quantitatively, we calculated the static stress field change due to water level rise. Our results show that impoundment of the TGR can cause high-stress changes in its vicinity and make the rocks closer to failure under a low internal friction angle ϕ (Fig. 7). Previous studies have shown that the frictional coefficient can be as low as 0.08 in water-saturated rocks, suggesting a low frictional angle of approximately 4.6° (e.g., Fulton et al., 2013). Hence, owing to strong perennial reservoir water and abundant precipitation (Huang et al., 2018; Tang et al., 2019), it is reasonable to use a low internal friction angle in this region. In addition, ΔF_{DP} shows similar patterns in the head area of the reservoir under the two background stress fields. However, when using the stress field of the head area (NE–SW), ΔF_{DP} was not consistent with the seismicity upstream of the TGR (Figs. 7e and 7f).

According to our calculation, we can hypothesize as to how water level affects seismicity near the reservoir (group-1 events). In the shallow part, earthquakes may be jointly modulated by the elastic response and pore pressure variations. However, in the deep part, the instantaneous elastic response plays a dominant role. In these places, the pore fluid pressure variations are weaker and probably become too insignificant to cause the rocks to fracture. This also leads to the pattern shown in Fig. 3c that deep earthquakes tend to occur directly below the TGR or close to the river bank, where the ΔF_{DP} amplitude is larger.

We used a 1D model to calculate the changes in pore pressure caused by seasonal precipitation. Based on this, we can reject the hypothesis that the pore pressure variations caused by precipitation drive group-2 events. Hainzl et al. (2006) suggested that the tiny pressure variations associated with precipitation can trigger seismicity at Mt. Hochstaufen because the crust there is close to failure. However, our study, to some extent, demonstrates that in the stable intraplate region, rainfall-induced pore pressure variations might not be a dominant factor modulating earthquakes. According to the synchronization signal, we assumed that the elastic response to the changes in precipitation-related surface water storage may be a possible mechanism for group-2 events. Because seasonal precipitation can cause large variations in surface loads, and thus may lead to greater stress variations than pore pressure (Bettinelli et al., 2008; Birhanu and Bendick, 2015; Dutilleul et al., 2021).

Changes in the surface hydrosphere can lead to different regional seismicity patterns. For example, in the Himalayas, California, and the northern Rocky Mountains, seismic productivity coincides with the stressing rate (Bettinelli et al., 2008; Johnson et al., 2017a; Perry and Bendick, 2021). However, in the TGR area, we reported earthquakes associated with stress perturbation (Fig. S15), similar to the cases in the New Madrid Seismic Zone and the western branch of the East African rift system (Craig et al., 2017; Xue et al., 2020). According to Ader et al. (2014), the variations in seismicity are predicted to be related to the peak stress if the amplitude of the cyclic load is the same order of magnitude as the secu-

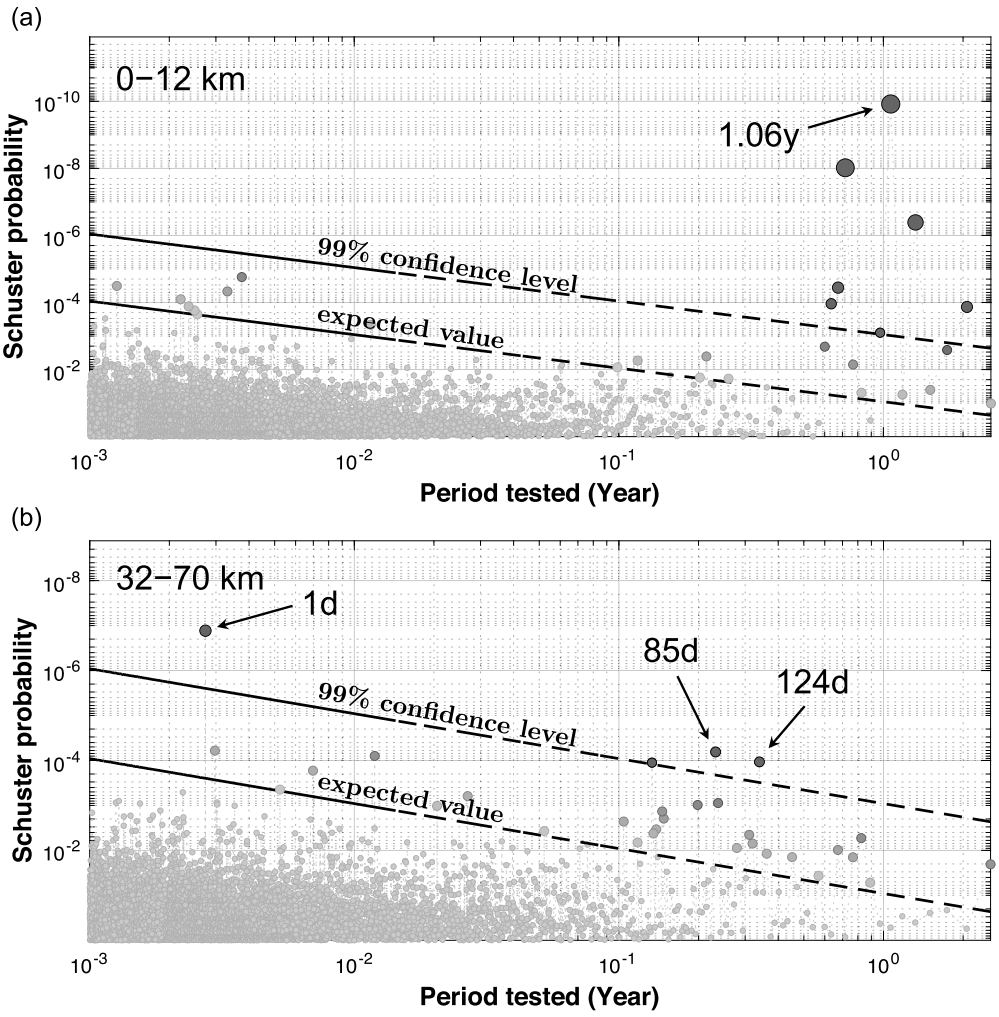

Fig. 5. Schuster spectra built with group-1 (a) and group-2 (b) declustered sub-catalogs. y: year. d: day.

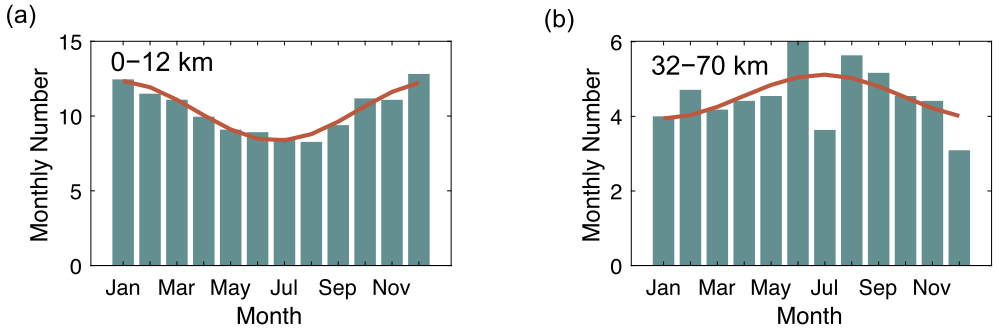

Fig. 6. Analysis of seasonal trends in seismicity in the TGR area. Green bars indicate the number of earthquakes per month in the group-1 (a) and group-2 (b) declustered sub-catalogs. Orange curves are the best-fit annual Fourier series to the stacked data.

lar stress rate multiplied by the duration. Therefore, we suggest a slow tectonic load rate and long critical nucleation period for the TGR area.

In this study, we could not exclude other possible combinations of different processes, such as atmospheric pressure, temperature changes, and solid tides (e.g., Cochran et al., 2004; Gao et al., 2000; Johnson et al., 2017b). In particular, we have not attempted to assess the impact of reservoir water-level changes on earthquakes that occur 32–70 km away from the TGR. Because this involves a common problem in current triggered-earthquake research: how far away from an operation site an earthquake can still be induced/triggered (Goebel and Brodsky, 2018). On the one hand, it has long been believed that the dangerous areas for induced/triggered earthquakes are concentrated in the vicinity of the operation (Foulger et al., 2018). Chen (2009) even judged that the 2008 Wenchuan earthquake was not triggered by the impoundment of the Zipingpu Reservoir, since the distance between the reservoir and the hypocenter was more than 5 km. On the other hand, many recent studies on injection-triggered seismicity (ITS) have shown that ITS may occur more than 30 km away from the wells (Goebel and Brodsky, 2018; Keranen et al., 2014). Nevertheless, no bimodal distribution pattern of spatial distance has been reported for reservoir-triggered seismicity cases worldwide. Moreover, it seems complicated to explain the different seismicity

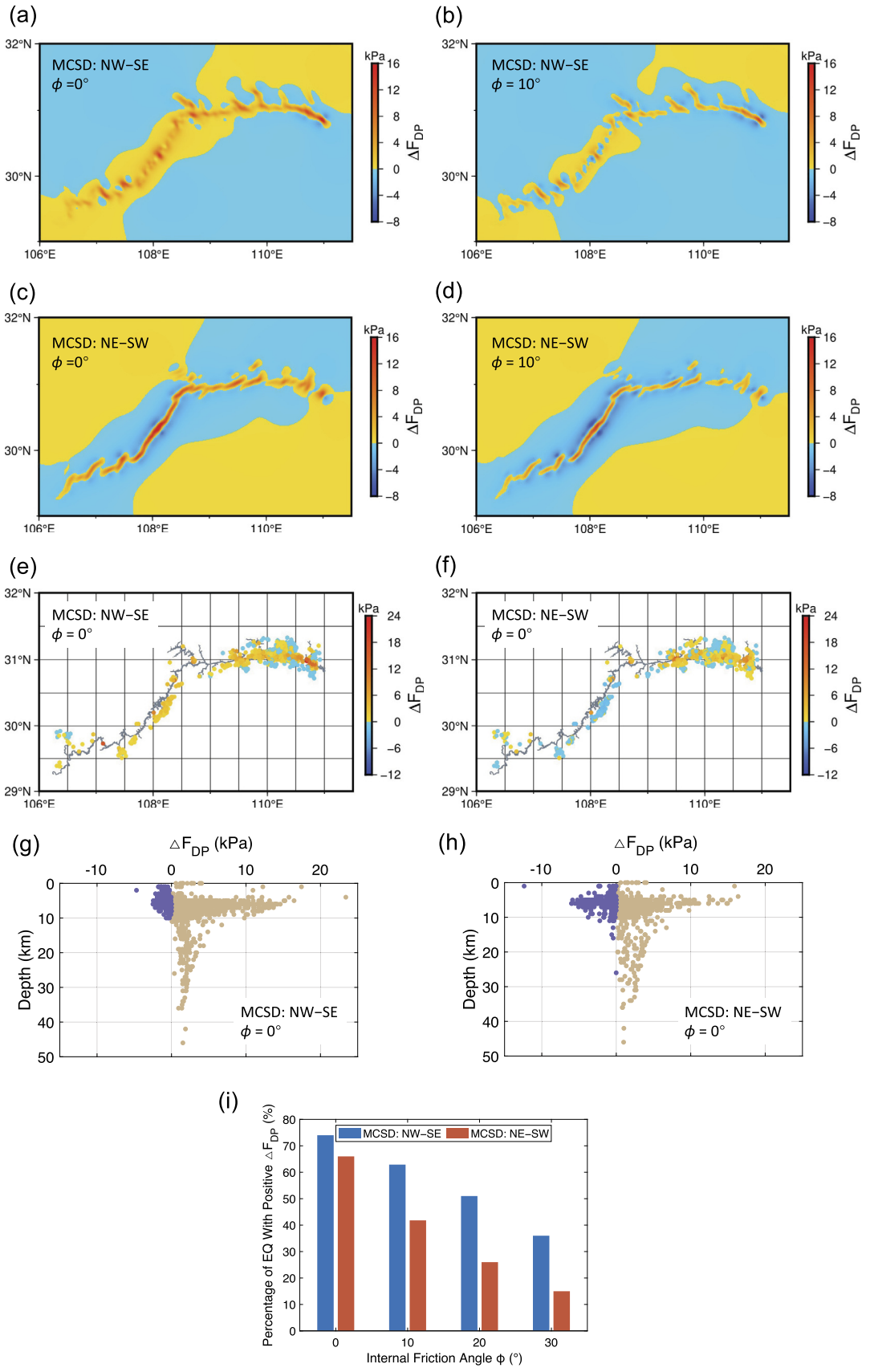

Fig. 7. Static elastic response to water-level rise (from 145 m to 175 m). (a, b) ΔF_{DP} values calculated at 6-km depth with the MCSD of NW–SE when $\phi = 0°$ and 10°. (c, d) ΔF_{DP} values calculated at 6-km depth with the MCSD of NE–SW when $\phi = 0°$ and 10°. (e, f) ΔF_{DP} calculated at the hypocenters of group-1 events when $\phi = 0°$ with the MCSD of NW–SE and NE–SW. (g, h) The relationship between ΔF_{DP} and focal depth when $\phi = 0°$ with the MCSD of NW–SE and NE–SW. The brown and purple scatter points represent the earthquakes with positive and negative ΔF_{DP}, respectively. (i) The proportion of group-1 earthquakes that had positive ΔF_{DP}. EQ: earthquakes. MCSD: maximum compressive stress direction.

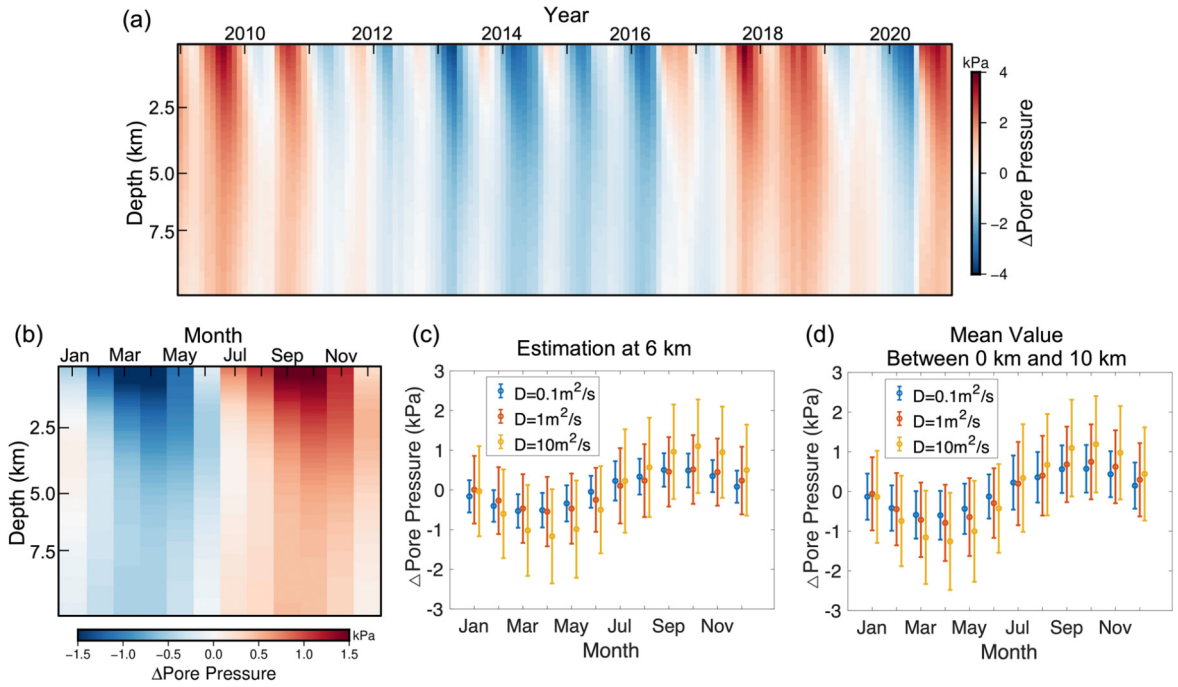

Fig. 8. Estimation of precipitation-induced pore pressure variations. The results were detrended. (a) Temporal evolution of pore pressure with depth when the hydraulic coefficient is 1.0 m^2/s. (b) Annual stacks of the pore pressure variations at different depths from July 2009 to June 2020 when the hydraulic coefficient is 1.0 m^2/s. (c) Seasonal pore pressure variations extracted at 6-km depth under different hydraulic diffusivity values, with the 1-standard deviation shown by the vertical bar. (d) Average pore pressure variations within 0–10 km, with 1-standard deviation shown by the vertical bar.

patterns in the three regions based on changes in reservoir water level. Overall, we are convinced that earthquakes occurring 0–12 km from the TGR are driven by the water level. Simultaneously, we are more inclined to believe that earthquakes that occur 32–70 km away from the TGR are modulated by other mechanisms, among which the change in precipitation-associated water storage is a potential candidate.

The seismicity may be modulated by the hydrosphere. The relevant processes are controlled by many factors, such as the initial stress state, pre-existing faults, hydraulic conductivity of fractures, and hydrodynamic properties of the underlying rocks (Bell and Nur, 1978; Huang et al., 2018). The TGR area has a large span, its geological structure is complicated, and the seismic risks in different regions vary greatly (Tang et al., 2019). In the future, further studies to establish a multi-field coupling geomechanical model and an earthquake-physics model would be challenging but worthwhile.

6. Conclusions

We examined seismicity characteristics in the Three Gorges Reservoir area since the third stage of the impoundment (2009–2020) and investigated their relationship with hydrosphere changes. The following conclusions can be drawn.

1) Seismicity in the TGR area is concentrated in two regions, within 0–12 km and 32–70 km from the TGR.
2) The productivity of earthquakes within 0–12 km of the TGR is enhanced in winter and reduced in summer. This is highly correlated with the reservoir water level. The instantaneous elastic response owing to changes in the reservoir water level plays a significant role.
3) Earthquakes occurring 32–70 km from the TGR show slightly opposite seasonal patterns, that is, they are less frequent in winter and more frequent in summer. The seismic productivity is moderately correlated with regional precipitation. The pore pressure variations due to precipitation are unlikely to be the main factor that modulate this group of earthquakes.

CRediT authorship contribution statement

Linxuan Li: Data curation, Formal analysis, Investigation, Methodology, Validation, Writing – original draft, Writing – review & editing. **Gang Luo:** Conceptualization, Formal analysis, Funding acquisition, Methodology, Supervision, Writing – original draft, Writing – review & editing.

Declaration of competing interest

The authors declare that they have no known competing financial interests or personal relationships that could have appeared to influence the work reported in this paper.

Acknowledgements

This study is funded by the National Key Research and Development Project of China (2021YFC3000605), the Open Foundation of the United Laboratory of Numerical Earthquake Forecasting (2020LNEF01), and the National Natural Science Foundation of China (41974107, 41574085). We sincerely appreciate Editor Jean-Philippe Avouac and two anonymous reviewers for incredibly constructive comments and suggestions that improve the manuscript. We thank Luciano Telesca for discussion on the Allan factor, Sebastian Hainzl for discussion on the pore-pressure modeling, Jia Cheng for discussion on the reliability of the earthquake catalog data, and Bao Zhang for providing the water loading data. We also appreciate the data support from China Earthquake Networks Center and the National Earthquake Data Center (http://data.earthquake.cn/), Yangtze River Hydrological Network (http://www.cjh.com.cn/), and China Meteorological Data Service Center (http://data.cma.cn/). The figures were plotted by MATLAB (http://www.mathworks.com/) and Generic Mapping Tools (Wessel et al., 2019).

Appendix A. Supplementary material

Supplementary material related to this article can be found online at https://doi.org/10.1016/j.epsl.2022.117618.

References

Ader, T.J., Avouac, J.P., 2013. Detecting periodicities and declustering in earthquake catalogs using the Schuster spectrum, application to Himalayan seismicity. Earth Planet. Sci. Lett. 377, 97–105. https://doi.org/10.1016/j.epsl.2013.06.032.

Ader, T.J., Lapusta, N., Avouac, J.P., Ampuero, J.P., 2014. Response of rate-and-state seismogenic faults to harmonic shear-stress perturbations. Geophys. J. Int. 198, 385–413. https://doi.org/10.1093/gji/ggu144.

Bell, M.L., Nur, A., 1978. Strength changes due to reservoir-induced pore pressure and stresses and application to Lake Oroville. J. Geophys. Res., Solid Earth 83, 4469–4483. https://doi.org/10.1029/JB083iB09p04469.

Bettinelli, P., Avouac, J.P., Flouzat, M., Bollinger, L., Ramillien, G., Rajaure, S., Sapkota, S., 2008. Seasonal variations of seismicity and geodetic strain in the Himalaya induced by surface hydrology. Earth Planet. Sci. Lett. 266, 332–344. https://doi.org/10.1016/j.epsl.2007.11.021.

Birhanu, Y., Bendick, R., 2015. Monsoonal loading in Ethiopia and Eritrea from vertical GPS displacement time series. J. Geophys. Res., Solid Earth 120, 7231–7238. https://doi.org/10.1002/2015jb012072.

Byerlee, J., 1978. Friction of rocks. Pure Appl. Geophys. 116, 615–626. https://doi.org/10.1007/BF00876528.

Chen, Y., 2009. Did the reservoir impoundment trigger the Wenchuan earthquake? Sci. China Earth Sci. 52, 431–433. https://doi.org/10.1007/s11430-009-0067-2.

Cochran, E.S., Vidale, J.E., Tanaka, S., 2004. Earth tides can trigger shallow thrust fault earthquakes. Science 306, 1164–1166. https://doi.org/10.1126/science.1103961.

Craig, T.J., Chanard, K., Calais, E., 2017. Hydrologically-driven crustal stresses and seismicity in the New Madrid Seismic Zone. Nat. Commun. 8, 1–11. https://doi.org/10.1038/s41467-017-01696-w.

Drucker, D.C., Prager, W., 1952. Soil mechanics and plastic analysis or limit design. Q. Appl. Math. 10, 157–165. https://doi.org/10.1090/qam/48291.

Dutilleul, P., Johnson, C.W., Burgmann, R., 2021. Periodicity analysis of earthquake occurrence and hypocenter depth near Parkfield, California, 1994-2002 versus 2006-2014. Geophys. Res. Lett. 48. https://doi.org/10.1029/2020gl089673.

Foulger, G.R., Wilson, M.P., Gluyas, J.G., Julian, B.R., Davies, R.J., 2018. Global review of human-induced earthquakes. Earth-Sci. Rev. 178, 438–514. https://doi.org/10.1016/j.earscirev.2017.07.008.

Fulton, P.M., Brodsky, E.E., Kano, Y., Mori, J., Chester, F., Ishikawa, T., Harris, R.N., Lin, W., Eguchi, N., Toczko, S., Expedition, S., Expedition, T.S., Expedition, K.R.S., 2013. Low coseismic friction on the Tohoku-Oki Fault determined from temperature measurements. Science 342, 1214–1217. https://doi.org/10.1126/science.1243641.

Gao, S.S., Silver, P.G., Linde, A.T., Sacks, I.S., 2000. Annual modulation of triggered seismicity following the 1992 Landers earthquake in California. Nature 406, 500–504. https://doi.org/10.1038/35020045.

Ge, S.M., Liu, M.A., Lu, N., Godt, J.W., Luo, G., 2009. Did the Zipingpu Reservoir trigger the 2008 Wenchuan earthquake? Geophys. Res. Lett. 36. https://doi.org/10.1029/2009gl040349.

Goebel, T.H.W., Brodsky, E.E., 2018. The spatial footprint of injection wells in a global compilation of induced earthquake sequences. Science 361, 899–903. https://doi.org/10.1126/science.aat5449.

Gonzalez, P.J., Tiampo, K.F., Palano, M., Cannavo, F., Fernandez, J., 2012. The 2011 Lorca earthquake slip distribution controlled by groundwater crustal unloading. Nat. Geosci. 5, 821–825. https://doi.org/10.1038/ngeo1610.

Hainzl, S., Ben-Zion, Y., Cattania, C., Wassermann, J., 2013. Testing atmospheric and tidal earthquake triggering at Mt. Hochstaufen, Germany. J. Geophys. Res., Solid Earth 118, 5442–5452. https://doi.org/10.1002/jgrb.50387.

Hainzl, S., Kraft, T., Wassermann, J., Igel, H., Schmedes, E., 2006. Evidence for rainfall-triggered earthquake activity. Geophys. Res. Lett. 33. https://doi.org/10.1029/2006gl027642.

Hu, X.P., Zang, A.N., Heidbach, O., Cui, X.F., Xie, F.R., Chen, J.W., 2017. Crustal stress pattern in China and its adjacent areas. J. Asian Earth Sci. 149, 20–28. https://doi.org/10.1016/j.jseaes.2017.07.005.

Huang, R., Zhu, L.P., Encarnacion, J., Xu, Y.X., Tang, C.C., Luo, S., Jiang, X.H., 2018. Seismic and geologic evidence of water-induced earthquakes in the Three Gorges Reservoir region of China. Geophys. Res. Lett. 45, 5929–5936. https://doi.org/10.1029/2018gl077639.

Jaeger, J.C., Cook, N.G.W., Zimmerman, R., 2007. Fundamentals of Rock Mechanics, fourth ed. Blackwell Publishing, Oxford.

Johnson, C.W., Fu, Y.N., Burgmann, R., 2017a. Seasonal water storage, stress modulation, and California seismicity. Science 356, 1161–1164. https://doi.org/10.1126/science.aak9547.

Johnson, C.W., Fu, Y.N., Burgmann, R., 2017b. Stress models of the annual hydrospheric, atmospheric, thermal, and tidal loading cycles on California faults: perturbation of background stress and changes in seismicity. J. Geophys. Res., Solid Earth 122, 10605–10625. https://doi.org/10.1002/2017jb014778.

Kagan, Y.Y., Jackson, D.D., 1991. Long-term earthquake clustering. Geophys. J. Int. 104, 117–133. https://doi.org/10.1111/j.1365-246X.1991.tb02498.x.

Keranen, K.M., Weingarten, M., Abers, G.A., Bekins, B.A., Ge, S., 2014. Sharp increase in central Oklahoma seismicity since 2008 induced by massive wastewater injection. Science 345, 448–451. https://doi.org/10.1126/science.1255802.

Lai, Y., Zhang, B., Yao, Y.B., Li, J.Y., 2022. Quantitatively analyzing the impacts of seasonal water storage changes in the Three Gorges Reservoir on nearby crust. Pure Appl. Geophys. 179, 817–831. https://doi.org/10.1007/s00024-021-02928-3.

Perry, M., Bendick, R., 2021. Intraplate seasonal seismicity in the northern rocky mountains of Montana and Idaho. Geophys. Res. Lett. 48. https://doi.org/10.1029/2020gl090371.

Schuster, A., 1897. On lunar and solar periodicities of earthquakes. Proc. R. Soc. Lond. 61, 455–465.

Talwani, P., Chen, L., Gahalaut, K., 2007. Seismogenic permeability, ks. J. Geophys. Res., Solid Earth 112. https://doi.org/10.1029/2006jb004665.

Tang, H.M., Wasowski, J., Juang, C.H., 2019. Geohazards in the three Gorges Reservoir Area, China lessons learned from decades of research. Eng. Geol. 261. https://doi.org/10.1016/j.enggeo.2019.105267.

Telesca, L., Fat-Elbary, R., Stabile, T.A., Haggag, M., Elgabry, M., 2017. Dynamical characterization of the 1982-2015 seismicity of Aswan region (Egypt). Tectonophysics 712, 132–144. https://doi.org/10.1016/j.tecto.2017.05.009.

Telesca, L., Thai, A.T., Cao, D.T., Ha, T.G., 2021. Spectral evidence for reservoir-triggered seismicity at Song Tranh 2 Reservoir (Vietnam). Pure Appl. Geophys. 178, 3817–3828. https://doi.org/10.1007/s00024-021-02858-0.

Thurner, S., Lowen, S.B., Feurstein, M.C., Heneghan, C., Feichtinger, H.G., Teich, M.C., 1997. Analysis, synthesis, and estimation of fractal-rate stochastic point processes. Fractals 5, 565–595. https://doi.org/10.1142/s0218348x97000462.

Wang, X.W., Chen, Y., Song, L.C., Chen, X.Y., Xie, H.J., Liu, L., 2013. Analysis of lengths, water areas and volumes of the Three Gorges Reservoir at different water levels using Landsat images and SRTM DEM data. Quat. Int. 304, 115–125. https://doi.org/10.1016/j.quaint.2013.03.041.

Wessel, P., Luis, J.F., Uieda, L., Scharroo, R., Wobbe, F., Smith, W.H.F., Tian, D., 2019. The generic mapping tools version 6. Geochem. Geophys. Geosyst. 20, 5556–5564. https://doi.org/10.1029/2019gc008515.

Wu, J.C., Chen, S.J., Cai, Y.J., Li, H., Lei, D.N., Yu, S., Qiao, Y.Q., Chen, Z.H., Liu, Z.F., 2012. Numerical simulation of equivalent stress field after the impoundment of the Three Gorges Reservoir and the seismogenic mechanism of Hujiaping Ms4.1 earthquake. J. Seismol. Res. 35, 42–47 (in Chinese).

Xue, L., Johnson, C.W., Fu, Y.N., Burgmann, R., 2020. Seasonal seismicity in the western branch of the East African Rift System. Geophys. Res. Lett. 47. https://doi.org/10.1029/2019gl085882.

Yi, L.X., Zhao, D., Liu, C.L., 2012. Preliminary study of reservoir-induced seismicity in the Three Gorges Reservoir, China. Seismol. Res. Lett. 83, 806–814. https://doi.org/10.1785/0220110132.

Zaliapin, I., Ben-Zion, Y., 2013. Earthquake clusters in southern California I: identification and stability. J. Geophys. Res., Solid Earth 118, 2847–2864. https://doi.org/10.1002/jgrb.50179.

Zhang, L.F., Li, J.G., Sun, X.D., Liao, W.L., Zhao, Y.N., Wei, G.C., He, C.F., 2018. A possible mechanism of reservoir-induced earthquakes in the Three Gorges Reservoir, central China. Bull. Seismol. Soc. Am. 108, 3016–3028. https://doi.org/10.1785/0120180015.

Zhang, Q.F., Lou, Z.P., 2011. The environmental changes and mitigation actions in the Three Gorges Reservoir region, China. Environ. Sci. Policy 14, 1132–1138. https://doi.org/10.1016/j.envsci.2011.07.008.

Zoback, M.D., 2007. Reservoir Geomechanics. Cambridge University Press, New York. https://doi.org/10.1017/CBO9780511586477.

Zoback, M.L., 1992. Stress-field constraints on intraplate seismicity in eastern North-America. J. Geophys. Res., Solid Earth 97, 11761–11782. https://doi.org/10.1029/92jb00221.